

All-atom simulations predict how single point mutations promote serpin misfolding

Authors: Fang Wang^{1,†}, Simone Orioli^{2,3,†}, Alan Ianeselli⁴, Giovanni Spagnolli⁴, Silvio a Beccara^{4,5}, Anne Gershenson^{6*}, Pietro Faccioli^{2,3*}, Patrick L. Wintrode^{1*}

Affiliations:

¹Department of Pharmaceutical Sciences, University of Maryland School of Pharmacy, Baltimore, MD 21201, USA.

²Physics Department, University of Trento, via Sommarive 14 Povo, Trento 38123, Italy.

³Trento Institute for Fundamental Physics and Applications (INFN-TIFPA), via Sommarive 14 Povo, Trento 38123, Italy.

⁴Center for Integrative Biology (CIBIO), University of Trento, via Sommarive 9 Povo, Trento 38123, Italy.

⁵European Centre for Theoretical Nuclear Physics and Related Areas (ECT*-FBK), Strada delle Tabarelle 287, Villazzano (Trento) 38123.

⁶Department of Biochemistry & Molecular Biology, University of Massachusetts, Amherst, MA 01003, USA.

*Correspondence to: pwintrod@rx.umaryland.edu, pietro.faccioli@unitn.it, gershenson@biochem.umass.edu

†These authors contributed equally to this work.

Abstract:

Protein misfolding is implicated in many diseases, including the serpinopathies. For the canonical inhibitory serpin α_1 -antitrypsin (A1AT), mutations can result in protein deficiencies leading to lung disease and polymerization prone mutants can accumulate in hepatocytes leading to liver disease. Using all-atom simulations based on the recently developed Bias Functional algorithm we elucidate how wild-type A1AT folds and how the disease-associated S (Glu264Val) and Z (Glu342Lys) mutations lead to misfolding. The deleterious Z mutation disrupts folding at an early stage, while the relatively benign S mutant shows late stage minor misfolding. A number of suppressor mutations ameliorate the effects of the Z mutation and simulations on these mutants help to elucidate the relative roles of steric clashes and electrostatic interactions in Z misfolding. These results demonstrate a striking correlation between atomistic events and disease severity and shine light on the mechanisms driving chains away from their correct folding routes.

Understanding how mutations alter protein misfolding propensities and the physico-chemical mechanisms underlying this shift is key to clarifying the molecular basis of many diseases. One set of relatively common protein misfolding diseases, the serpinopathies, arise when mutations in inhibitory serpins lead to misfolding, thus reducing the secreted levels of these important protease inhibitors¹. Mutations in the canonical secretory serpin α_1 -antitrypsin (A1AT) result in the most common serpinopathies, the α_1 -antitrypsin (A1AT) deficiencies. In A1AT deficiencies, low circulating A1AT levels dysregulate leukocyte serine proteases resulting in lung disease which can be slowed but not halted by A1AT augmentation therapy². Extremely pathogenic A1AT mutations, such as Z (Glu342Lys), can lead to both lung disease, due to loss of function, and liver disease, due to A1AT accumulation in the endoplasmic reticulum (ER) of hepatocytes, which generate most of the circulating A1AT. With the exception of liver transplants, there are no effective treatments for A1AT associated liver disease³.

In vitro, the pathogenic A1AT Z mutant folds very slowly, spending hours in at least one partially folded intermediate state⁴. Similarly, Z secretion from cells is slow and, while some Z species are targeted for degradation⁵⁻⁷, misfolded Z accumulates in the ER where it can polymerize⁸. Despite numerous experimental studies⁹⁻¹³, little is known about the structure of misfolded species for any A1AT disease-associated mutant, hindering efforts to either rescue the folding of these species or to target them for degradation.

Molecular dynamics (MD) simulations offer an attractive approach to study protein folding and misfolding, as they can in principle reveal folding pathways and intermediates in atomistic detail. To date the application of all-atom MD simulations to investigate protein folding and misfolding has been limited to small single-domain proteins, with relatively short folding times. In particular, recent developments such as the Anton special-purpose supercomputer¹⁴ and the massively distributed folding@home project¹⁵ have made it possible to generate *in silico* several reversible folding/unfolding events for a number of small globular proteins (< 100 amino acids) with folding times up to the ms range. These studies have demonstrated that current all-atom force fields in explicit solvent can lead to the correct native states of proteins and predict with good accuracy their folding kinetics. Unfortunately, most biologically relevant proteins are much larger than 100 amino acids and have folding times as long as seconds and beyond. In particular, A1AT and other serpins contain approximately 400 amino acids and fold over tens of minutes^{9,12,13}. Due to their large size and slow folding kinetics, simulating serpin folding with conventional MD simulations is not feasible, even using the most powerful available supercomputers.

In this work, we rely on a recently developed variational method called the Bias Functional (BF) approach (see Methods) to overcome this limitation. We use this scheme to characterize the folding and misfolding of wild-type (WT) A1AT, the pathological Z mutant and the relatively benign S (Glu264Val) mutant¹, starting from several fully denatured configurations. The results of these all-atom simulations provide testable, atomistic models for how WT A1AT folds, how disease associated mutants misfold and how suppressor mutations can rescue misfolding. These results also shine light on the connections between single-point mutations and the pathogenicity of

misfolding prone proteins, and provide physical mechanisms responsible for misfolding phenotypes.

Results and Discussion

The BF approach. Using the BF algorithm¹⁶ it is feasible to use standard computer clusters to generate many folding and misfolding events for proteins as large as serpins, using state-of-the-art all-atom force fields. This algorithm identifies the most realistic reaction pathways within an ensemble of uncorrelated trial trajectories, generated by the so-called ratchet-and-pawl MD (rMD)^{17,18}. In rMD, a biasing force is introduced only when the chain tends to back-track towards the unfolded state and it is not applied when the chain spontaneously progresses towards the native state. In the BF approach a rigorously derived variational condition is applied to identify the trial rMD pathways which have the largest probability to occur in the absence of any bias. In the following, we shall refer to these paths as Minimum Bias Trajectories (MBTs).

The accuracy of *all* variational approaches critically depends on the quality of the model subspace, i.e. the set of possible solutions, within which the optimal approximate solution is identified through the variational condition. In the BF approach, the model subspace is defined by the trial folding trajectories generated using the rMD protocol. Since a suboptimal choice of the model subspace may introduce uncontrolled systematic errors, variational approaches must be carefully benchmarked against exact methods and extensively validated against experimental data.

The BF method was benchmarked against the results of MD folding simulations, performed using the Anton supercomputer^{16,19}, where both methods used the same all-atom force field. In particular, the folding mechanism and the precise order of native contact formation during the folding of an all-beta protein (WW domain Fip35) and of an all-alpha protein (villin headpiece subdomain) predicted by the BF method were found to be statistically indistinguishable from those obtained using conventional MD methods. The predictions of the BF approach have also been validated against experimental data. For example, the BF method was used to study the folding of two alpha proteins consisting of nearly 100 amino acids (IM7 and IM9), with highly homologous native structures, but very different folding kinetics²⁰. The BF method correctly reproduced all of the observed kinetic features.

In a very recent investigation, the BF approach has been interfaced with quantum electronic structure calculations to yield a direct prediction of the expected time-resolved near and far UV circular dichroism (CD) spectra in the folding of canine lysozyme. The BF results agree with the experimental data, correctly predicting the existence of a folding intermediate and reproducing the difference between the intermediate and native state CD spectra, both in the near UV, which reports on protein secondary structure, and in far UV, which reports on the local environment of aromatic residues, particularly tryptophans (PF, unpublished data).

An early version of the BF algorithm (called dominant reaction pathway or DRP) was also successfully applied to sample the conformational transition leading to serpin latency²¹. These BF calculations correctly reproduce the effects of point mutations on the reaction kinetics and provide an atomistically detailed picture which explains why binding a specific small molecule accelerates the latency transition of the serpin plasminogen activator inhibitor (PAI-1). This study also delineates differences between the PAI-1 latency transition and that of A1AT to help explain why PAI-1 easily accesses the latent state while A1AT does not.

In order to further explore serpin conformational changes and to validate the BF simulation results, we begin the present study by simulating and analyzing the folding of the WT A1AT. We compare the results of the simulations to available experimental results and provide new, *testable* atomistically resolved data on how WT A1AT folds. These WT simulations also provide the reference for comparing folding and misfolding pathways. We therefore proceed to simulate and analyze the folding of disease associated A1AT variants and suppressor mutants.

WT A1AT folding pathways. For all of the A1AT variants, folding starts with the independent formation of local structures (Fig. 1A, stage 1) that we refer to as foldons, following the usage of Wolynes, Englander and coworkers^{22,23}. In the majority of successful WT trajectories, foldons dock in a well-defined order, as determined from visual inspection, from the plot of the radius of gyration versus fraction of native contacts and from an automated statistical analysis that identifies the most relevant change-points²⁴ (Fig. 1A).

In WT MBTs, early native interactions are formed between residues at the top of strands 5/6A (s5/6A) in the nascent sheet A and the nascent B-C barrel formed by parts of strands 3C, 4C and 1 to 3B (Fig. 1A, stage 2). In particular, a hydrogen bond is formed between Glu342 and Thr203 and van-der-Waals interactions are established between Pro289 and Met residues 220 and 221. The structures corresponding to stages 1 (foldon formation) and 2 (early inter-foldon interactions) in Figure 1A were subjected to 200 ns of conventional MD simulations in explicit solvent. In these MD simulations, the C-terminal β -hairpin formed by strands 4/5B is not stable consistent with the experimental finding that the isolated peptide containing the 36 C-terminal A1AT residues lacks stable structure in the absence of the rest of the protein²⁵. In contrast, as shown in Fig. 2A, the three N-terminal foldons and the network of interactions between the nascent B-C barrel and s5/6A are stable on the time scale of these conventional MD simulations.

In most WT trajectories (see Movie S1), non-native interactions between the loop at the top of strand 3A and β -strands 2 and 3B prevent correct positioning of the B-C barrel leading to the first barrier (Fig. 1A, stage 3). Disruption of this steric hindrance allows for the correct positioning of the B-C barrel and docking of s5/6A to s1-3A thus completing β -sheet A formation (Fig. 1A, stage 4). At this stage, the C-terminal β -hairpin (s4/5B) and the N-terminal helices are solvent exposed and free to move on flexible linkers. Folding completes when the C-terminal hairpin docks to

strands 1 to 3B (Fig. 1A, stage 5) followed by packing of the N-terminal helices and s6B on the back of the β sheets.

Our finding that completion of sheet A precedes C-terminal hairpin incorporation into sheet B agrees with fragment complementation studies, where docking of a fragment containing the C-terminal hairpin with a larger N-terminal A1AT fragment requires the presence of s5A¹¹ and thus, presumably, completion of sheet A. Similarly, in kinetic refolding experiments monitored by oxidative labeling of sidechains or hydrogen/deuterium exchange of backbone amides detected by mass spectrometry (MS), s5A is one of the last regions to acquire native-like protection^{12,13}. These same MS based studies found that s4B remains solvent exposed until late in the folding process, consistent with the late packing of the C-terminal hairpin (s4/5B) seen in our simulations.

WT A1AT contains two Trp residues, 238 in strand 2B, and 194, C-terminal to strand 3A in the "breach" region at the top of sheet A. Studies of A1AT single Trp mutants, in the WT background, show that during equilibrium unfolding, Trp194 is sensitive to the native to intermediate transition and that both Trp194 and Trp238 are sensitive to the intermediate to unfolded transition²⁶. In addition, stopped flow studies of WT A1AT refolding monitored by Trp fluorescence emission reported at least three kinetic phases for A1AT WT refolding, a very fast, ~50 ms, phase; a slower, ~500 ms, phase and a very slow 100s of seconds long phase⁹. Consistent with these data, in the WT A1AT BF folding simulations, Trp238 is buried early, in stages 1 & 2, as the foldons and nascent B-C barrel form (Fig. 1B) while consolidation of the breach and Trp194 burial and quenching, presumably by Tyr244, occurs later, when sheet A fully forms (Fig. 1A stage 4 and Fig. 1B). Trp194 is fully buried in the second to last folding step when the C-terminal hairpin inserts into sheet B correctly positioning the RCL. Thus the BF folding simulations results are in qualitative agreement with results from A1AT folding experiments monitored by Trp fluorescence emission.

While A1AT has only a single Cys residue and no disulfide bonds, folding studies of two serpins containing disulfide bonds, ovalbumin and antithrombin III, show that N-terminal disulfide bond formation and rearrangements occur after the C-terminus packs^{27,28}. These experimental results imply that the N-terminus is involved in the final stage of serpin folding. The large conformational transition performed by the N-terminal foldon in the last stage of WT A1AT folding suggests that the last steps in A1AT, ovalbumin and antithrombin III folding are similar and provides a *testable*, atomistically detailed explanation for the experimental results.

The BF WT A1AT folding simulations are in good agreement with existing serpin folding data and set the stage for generating detailed models of mutation induced serpin misfolding.

Misfolding of A1AT disease-associated variants. BF folding simulations for the S (Glu264Val) and Z (Glu342Lys) mutants suggest that these two A1AT variants misfold differently. To effectively analyze the differences between WT, S and Z folding and misfolding for these non-equilibrium BF folding simulations we focused on the observation that mutants with a higher

misfolding propensity are less likely to reach configurations in which almost all of the native contacts have been formed. To quantify this measure for each A1AT variant, we used all of the frames from all of the minimum biased trajectories (MBTs) generated for each A1AT variant to construct a histogram describing how often each variant visits configurations with a given fraction of native contacts, Q (Fig. 3A). Comparisons between such histograms for WT and Z simulations correctly predict that the pathological Z mutant is significantly less able to populate structures close to the native state. In fact, none of the Z mutant MBTs successfully reached the fully folded state. In contrast, the Q histograms for S and WT trajectories are similar, consistent with the observation that the S mutation has only mild effects on A1AT folding¹ (Fig. 3A).

The Z mutation disrupts a network of electrostatic and hydrogen-bonding interactions at the top of β -sheet A (Fig. 3B). Experimentally, Z misfolding can be rescued by mutating Lys290 to Glu²⁹ leading to a reversed version of the original salt bridge (K290E/E342K or Glu/Lys) and reducing the probability of steric clashes. Consistent with experiment, our Glu/Lys simulations show a WT like distribution of native contacts (Fig. 3A).

One way to test the relative roles of electrostatics and sterics in Z misfolding is to place Glu at both 342 and 290 (K290E/E342 or Glu/Glu) thus preserving the electrostatic repulsion present in Z but reducing the side chain length. Consistent with cellular studies, where Z and Glu/Glu shows approximately 20% and 75% secretion efficiency, respectively, relative to WT A1AT³⁰, the distribution of native contacts in the Glu/Glu simulations resembles that of WT (Fig. 3A, Movie S2). The fact that both experiments and computations indicate that Glu/Glu can fold with reasonable efficiency suggests that the 290/342 salt bridge may not be essential for A1AT folding. To further test this hypothesis we determined whether replacing Lys290 with Ser could rescue Z (K290S/E342K or Ser/Lys) simply by alleviating steric clashes. The resulting MBTs are more WT-like than Z-like (Fig. 3A).

Investigating the order of contact formation. Does misfolding of A1AT mutants occur because some key native contacts are formed in the wrong order? To answer this question, we performed a statistical analysis based on the distribution of path similarity s introduced in¹⁸ and defined in the Methods. This parameter is equal to 1 when native contacts in two reactive trajectories are formed in exactly the same order, whereas $s=0$ when the order is entirely different. For completely random sequences of native contact formation the similarity distribution is sharply peaked around 0.3. Path similarities calculated between MBTs for the same variant (self-similarity) or between trajectories of different variants (cross similarity) are shown in Fig 4. For any given A1AT variant the self-similarity distribution obtained from all of the MBTs peaks around 0.6 (Fig. 4A). In contrast, comparisons between different variants show that Z MBTs differ significantly from WT (peak $s\sim 0.4$), while S and WT pathways are similar (peak $s\sim 0.6$) (Fig. 4B).

Path similarity analyses also indicate that while mutations at Lys290 may suppress Z misfolding, the paths are very different for different combinations of residues at positions 290 and 342. Folding of the Glu/Glu variant, where Lys290 is mutated to Glu in the WT background providing an

anionic charge repulsion between residues 290 and 342 compared to the cationic repulsion in the Z mutant, is most WT-like. The folding of the Ser/Lys variant diverges the most from WT, while the order in which contacts are formed in Glu/Lys - the charge-reversed salt-bridge in the Z background - span a large range from WT-like to quite different (Fig. 4B). These results, and the finding that in the BF folding simulations all of these salt-bridge variants are more likely to fold than Z, suggest that A1AT can fold using a number of alternative folding pathways. Moreover, they show that the Lys290-Glu342 salt-bridge, while not required for folding, is important for increasing the probability of the major folding mechanism observed in the WT A1AT BF folding simulations.

In S and WT trajectories, misfolding occurs late, resulting from premature docking of the N-terminal helices, which leaves the C-terminus solvent exposed (Fig. 5, Movie S3). Premature docking of the N-terminal helices to the rest of A1AT is essentially irreversible in the BF simulations due to the number of native contacts gained in these interactions. However, in experiments this misfolding may be reversible, and in cells interactions between the lectin chaperones and the N-terminal glycans at Asn residues 46 and 83 could help protect against this late misfolding.

In striking contrast, Z and WT folding diverge much earlier (Movie S4). As discussed above, the Z mutation replaces a conserved salt bridge between Lys290 and Glu342 (Fig. 5) with a charge-charge repulsion. This mutation appears to disrupt early native and non-native interactions between β -strands 5/6A and the B-C barrel. Electrostatic repulsion and steric hindrance, due to the length of the two Lys sidechains (K290/E342K), increase the probability that these residues assume a non-native spatial orientation. In contrast to Z, Glu/Glu achieves WT like docking between s5/6A and the B-C barrel despite the electrostatic repulsion between the two Glu residues. This supports the hypothesis that sterics, in addition to electrostatics, play a key role in Z misfolding.

In conclusion, our calculations provide a coherent atomistic and physics-based picture of serpin folding and misfolding. For WT A1AT, we find that there is a major folding pathway that begins with the initial assembly of local structural units, followed by higher order associations, some of which involve non-native contacts. The pathway ends with the incorporation of the C-terminal β -hairpin followed by docking of the N-terminal helices. These findings are supported by existing experimental data^{9-13,26-30} and the detailed molecular mechanisms provided here are experimentally testable. The multi-dimensional free energy landscape for folding is complex and, as exemplified by the Z suppressor mutants, there are alternative ways to successfully fold to the native state. Our simulations of pathological and suppressor mutants also elucidate the mechanism of Z misfolding and make the prediction that misfolding occurs early in the folding process, a prediction that should be amenable to experimental testing.

The scheme presented in this work opens a way to investigate many important disease-associated processes, which occur over minutes or hours, using only ordinary medium-sized computer clusters of the type available to most computational laboratories.

Methods:

The computational limitations of conventional MD have motivated the development of more sophisticated algorithms and approximations to study rare biomolecular transitions. Among these, well-tempered meta-dynamics has proved to be a powerful tool to profile the potential of mean-force of the slowest collective variables in a system³¹. Conversely, transition paths sampling³² offers a framework to directly sample reaction pathways, while transition interface sampling³³ and milestoning³⁴ enable the investigation of reaction kinetics. Unfortunately, to our knowledge, none of these powerful equilibrium and non-equilibrium methods have been successfully applied to reactions as complex and slow as serpin folding and misfolding.

The Bias Functional approach. In the BF approach a set of variationally optimized trajectories connecting an ensemble of fully denatured serpin configurations to folded and misfolded configurations is obtained through the following three-step procedure, schematically represented in Fig 6.

Step 1: Generation of initial denatured configurations. We sampled an ensemble of fully unfolded configurations (with a fraction of native contacts, $Q < 0.1$) by performing thermal unfolding MD simulations at 1600 K for 10 ns with an integration time of 1 fs starting from the WT native structure. Thermal unfolding was followed by a 10 ns relaxation at room temperature, T=300 K.

Step 2: Generation of trial folding and misfolding pathways: From each unfolded configuration X_i obtained at step 1, we initiated 12 rMD simulations. In rMD, the standard MD at room temperature T is modified by adding an unphysical history-dependent biasing force F_{rMD}^i defined as follows.

$$\mathbf{F}_{rMD}^i(X, t) = \begin{cases} -k_R \nabla^i z(X)(z[X(t)] - z_m(t)), & \text{for } z[X(t)] > z_m(t) \\ 0, & \text{for } z[X(t)] \leq z_m(t). \end{cases} \quad (1)$$

In this equation, $z(X)$ is a collective variable that measures the distance between the protein's instantaneous contact map $C_{ij}(X(t))$ and a reference contact map, calculated from the native state crystal structure X^{native} , i.e., $z[X(t)] = \sum_{i < j} [C_{ij}[X(t)] - C_{ij}(X^{native})]^2$. C_{ij} is a function of the distance between atom i and j, which interpolates between 0 and 1 and provides a continuum representation of the contact map $C_{ij}(X) = [1 - (r_{ij}/r_0)^6]/[1 - (r_{ij}/r_0)^{10}]$, where $r_0=0.75$ nm. The variable $z_m(t)$ in Equation (1) denotes the minimum value assumed by the collective coordinate z up to time t along the given rMD trajectory. Thus, the biasing force (Eqn. (1)) remains latent (equals 0) any time an rMD step leads to no change or to an increase of the overlap between the instantaneous and the native contact maps, i.e. if $z(X(t+\Delta t)) \leq z_m(t)$. On the other hand, the bias switches on whenever an elementary integration step leads to a decrease of the overlap with the native state, i.e. for $z(X(t+\Delta t)) > z_m(t)$.

Step 3: Identification of the least-biased transition pathways. The rMD paths generated in Step 2 are all affected by the presence of the unphysical biasing force \mathbf{F}_{rMD}^i . However, it can be rigorously shown¹⁶ that the trajectories in this trial path ensemble with the largest probability to occur in an

unbiased Langevin simulation are those with the least value of the so-called bias functional:

$$T[X] = \int_0^t d\tau \sum_{i=1}^N \frac{1}{\gamma_i m_i} |\mathbf{F}_{rMD}^i(X; \tau)|^2. \quad (2)$$

where γ_i and m_i denote the viscosity and mass of the i -th atom, respectively.

Thus, for each denatured condition X_i we retain only one minimum-bias trajectory and discard all other trial rMD paths. This procedure keeps to a minimum the systematic errors introduced by the biasing force.

It is important to emphasize that in rMD the progression towards configurations with increased numbers of native contacts occurs in an unbiased way, so that partially folded and misfolded structures are predictions of the underlying force field.

Force Fields. MD and rMD simulations were performed using the AMBER ff99SB force field³⁵, within the Generalized Born scheme implemented in GROMACS 4.5.2³⁶. Trial trajectories were generated by running 30 ns of rMD simulations at room temperature, 300 K, with an integration time of 1 fs. The parameter k_R in Equation (1), setting the strength of the biasing force, was 0.02 kJ/mol.

Simulations Details. The X-ray crystal structure of active, native wildtype (WT) α_1 -antitrypsin (A1AT) from Elliott and co-workers³⁷ (PDB: 1QLP) was used as the target structure for WT BF folding simulations. To our knowledge, the first 22 amino acids are disordered in all published A1AT structures. Thus, the sequences for the folding simulations start at Phe23. We note that, from a kinetic point of view, this active native state is only metastable. Indeed, A1AT spontaneously performs an irreversible conformational reaction into a fully stable, yet biologically latent structure with a mean-first-passage time on the order of days to weeks. The latency transition was previously characterized in atomistic detail using a variant of the BF algorithm²¹.

For all A1AT mutants, single point mutations were introduced using the mutator function in VMD³⁸. After we began our simulations, an X-ray crystal structure of the Z mutant was published, PDB: 5IO1³⁹. There are no significant differences between the WT and Z active, native structures. A structural alignment of our target Z structure with the published structure shows a root mean square deviation (RMSD) of 0.6 Å and the native contact maps are identical.

For simulation of WT folding we generated 12 independent fully denatured configurations by thermal unfolding at 1600 K. From each such condition we produced 48 trial rMD trajectories and extracted the MBT using the minimum bias condition, i.e. selecting the path with the least BF functional, defined in Eq. (2). Typically, for such a number of trial trajectories the requirements for convergence described in Ref. (16) are satisfied. For Z, S, and other A1AT variants, we also began each BF simulation with 12 independent unfolded configurations.

Even under the effect of the rMD biasing force, a residual degree of frustration persists. As a result, only 2% of our short WT A1AT MBTs reach the fully folded structure within the simulated time window. The majority of MBTs reach a fraction native contacts of at least 0.4, corresponding to the formation of the local foldons (Fig. 1A, stage 2A). 45% of all WT MBTs reach stage 4 or 5 shown in Figure 1A, where the central β -sheet A is fully formed and all that remains is the docking of the N and C termini.

We observed that all of the final folded A1AT structures generated by the BF simulations have a single strand crossover between strands 3 and 4C that is reversed relative to the X-ray crystal structure of active, metastable A1AT (PDB: 1QLP³⁷), see Fig. 7. This crossover involves just *two* residues and does not affect the total fraction of native contacts.

Standard MD simulations were started from representative frames taken from the BF trajectories. The structure was solvated with TIP3P water⁴⁰ and sodium and chloride ions were added to neutralize the system. Simulations were carried out at 300 K using periodic boundary conditions and the CHARMM36 force field⁴¹. Electrostatics were calculated using the Particle Mesh Ewald method⁴². Titratable groups were assigned protonation states for pH 7.0. The energy minimized system was heated to 300 K in 10 degree increments followed by a production run of 200 ns.

Change-Point Analysis: To identify the main transition points of the WT folding trajectory we adopted the multivariate change-point analysis introduced in reference 24 and implemented in the SIMPLE algorithm, developed by DE Shaw Research. This method is based on a statistical analysis of multi-dimensional time series extracted from atomistic trajectories. In particular, from one of our WT atomistic folding trajectories obtained using the BF approach, we extracted the evolution of the distances r_{ij} between all alpha-carbons i and j which are in contact in the native state. For each of such pairs of residues we computed the time series of the function of d_{ij} which interpolates smoothly between 0 and 1:

$$d_{ij} = \frac{1 - (r_{ij}/r_0)^6}{1 - (r_{ij}/r_0)^{10}} \quad (3)$$

Where $r_0=0.75$ nm is a fixed reference distance. The sensitivity parameter λ of the change-point analysis (see reference 24) has been set to 7500 in order to yield four conformational change points.

Fraction of Native Contacts Distribution: The frequency histograms of values of Q visited by the MBTs were obtained according to the following procedure. Let us consider a dataset composed of trajectories obtained from MD or BF simulations. For the whole collection trajectories we are interested in computing the fraction of native contacts, defined as

$$Q_0 = \sum_{i < j+3}^R C_{ij}^{\text{binary},0} \quad Q(t) = \frac{1}{Q_0} \sum_{i < j+3}^R C_{ij}^{\text{binary}}(t) \quad (4)$$

where R is the number of residues, $C^{\text{binary},0}$ is the binary contact map of the native structure, $C^{\text{binary}}(t)$ is the binary contact map at time t and Q_0 is the total number of native contacts in the active crystal structure. The probability of finding, among all the trajectories, a particular configuration identified by a fraction of native contacts is provided by

$$p(Q) = \frac{\sum_{T=1}^M \left[\sum_Q \delta(Q - \bar{Q}) \right]_T}{\int dQ \sum_{T=1}^M \left[\sum_{\bar{Q}} \delta(Q - \bar{Q}) \right]_T} \quad (5)$$

where the sum is extended over all M trajectories. In practice, the Dirac delta is smeared and computed by choosing a fixed bin width and counting how many configurations fall within Q and $Q+dQ$ for each trajectory in the set. This discrete distribution clearly shows which regions of native contacts are highly populated and which are rarely populated, thus giving an explicit indication of possible barriers to folding and the ability of a set of trajectories to reach, for example, the native state.

Path Similarity Analysis: The similarity parameter measures the consistency of the temporal succession in which native contacts are formed in two given pathways. The parameter takes on values ranging from 0 for no similarity, to 1 when all native contacts form in exactly the same succession for the two trajectories.

To compute this quantity, we define a matrix M which describes the order of native contact formation between atoms. Given as the time of formation of the i -th native contact in the k -th trajectory, the matrix element of the k -th path is defined as:

$$M_{ij}(k) = \begin{cases} 1 & \text{if } t_{ik} < t_{jk} \\ 0 & \text{if } t_{ik} > t_{jk} \\ \frac{1}{2} & \text{if } t_{ik} = t_{jk} \end{cases} \quad (6)$$

The similarity parameter is thus defined as

$$s(k, k') = \frac{1}{N_c(N_c - 1)} \sum_{i \neq j} \delta(M_{ij}(k) - M_{ij}(k')) \quad (7)$$

where N_c is the total number of native contacts. To provide a robust indication of the degree of heterogeneity of multiple trajectories, we can also compute the distribution of s , path similarity, over all possible pairs of trajectories, defined as

$$p(s) = \sum_{k < k'} \delta(s - s(k, k')) \quad (8)$$

The path similarity calculation allows us to quantitatively compare trajectories for a single A1AT variant, e.g., to determine similarities and differences between WT folding trajectories, and to determine whether and when the folding of A1AT mutants diverges from WT-like folding.

Acknowledgements: This work was funded by the Alpha-1 Foundation (PLW, PF) and NIH grant GM094848 (AG). We thank DE Shaw Research for help with the change-point analysis.

Author Contributions: F.W. designed, performed and analyzed the simulations and wrote the paper; S.O. analyzed the simulations and, as required, developed new analysis methods, and wrote the paper; A.I. & G.S. analyzed the simulations and, as required, developed new analysis methods; S.a B. designed and wrote the software to perform BF simulations; P.F. designed and analyzed simulations, developed new analysis methods as necessary and wrote the paper; A.G. & P.L.W. designed and analyzed simulations and wrote the paper.

Figure 1. A) Changes in the WT radius of gyration, R_g , as a function of native contacts formed along a typical successful WT folding trajectory. Change-points²⁴ are indicated by red diamonds. The A1AT structure colored by foldon and indicating the locations of the Z and S mutations and Lys290 is shown on the upper right. B) Solvent Accessible Surface Area (SASA) for the two Trp residues and relative distance between Trp194 and Tyr244, averaged over all successful WT A1AT folding pathways. Averages are represented by solid lines and standard deviations are represented by shaded areas. Locations of Trp 194 (red) and Trp238 (purple) are shown at the lower left.

Figure 2. A) Stability of A1AT foldons. The structure from 1A stage 1 in Figure 1A after 200 ns of conventional MD simulations in explicit solvent. The three foldons in the N-terminal two-thirds of A1AT are stable on this time scale. B) Stability of the contacts between s5/6A and the B-C barrel (spheres) after 200 ns of standard MD simulation in explicit solvent. Glu342, red; Lys290, blue; Pro289, yellow; Met220 and Met221, green; Thr 203, grey. The ribbon structure is colored by foldon as described in the main text.

Figure 3. A) Comparisons of the fraction of native contacts, Q , formed during folding and misfolding MBTs. For the indicated variants with N total MBTs, histograms were calculated using all frames from all N trajectories. The data for Z (E342K, $N=58$) and S (E264V, $N=35$) are in purple and blue respectively. Suppressor variants with mutations at residues 290 and/or 342 are Glu/Glu (K290E/E342, $N=25$), Glu/Lys (K290E/E342K, $N=40$) and Ser/Lys (K290S/E342K, $N=48$) in orange, gray and pink, respectively. In all of the histograms, the WT ($N=285$) data are in green. B) Close up view of the network of electrostatic and hydrogen-bonding interactions formed by Glu342 in WT A1AT.

Figure 4. Distributions of path similarities for WT and mutants (see Methods). The vertical dotted line indicates the average similarity score for two random sequences of native contact formation. Self-similarities are shown in A. Differences between the WT paths and the various mutant paths are shown in B. The coloring is the same as in Figure 2A.

Figure 5. A) The divergence of WT and Z folding with close up views of the region containing residues 290 and 342 (E: red and K: blue) and P289 (yellow) with T203, M220 and M221 in green. Glu/Glu is also shown. B) Representative misfolded structures for Z, S, and WT.

Figure 6. Schematic representation of the BF algorithm. Black solid lines are trial rMD trajectories obtained starting from configurations in the unfolded set U (blue) generated in Step 1. The dashed yellow line is the minimum bias path, for which the value of the bias functional T given in Equation (2) is least.

Figure 7. Non-native conformation in the gate region of A1AT. The crystal structure of native A1AT (PDB: 1QLP³⁷) is shown in cyan. The final structure from a representative WT minimally biased trajectory (MBT) that reaches the folded, native state is shown in green. As shown in the figure, in the native structure s4C passes over s3C while the reverse occurs in the successful BF

WT folding trajectories. This difference in twist affects *only* the contacts at the crossover points.

Supplementary Information

Movie S1: BF simulation of successful WT A1AT folding.

Movie S2: BF simulation of the successful folding of the Glu/Glu (Lys290Glu/Glu342) A1AT variant.

Movie S3: BF simulation of S (Glu264Val) A1AT misfolding

Movie S4: BF simulation of Z (Glu342Lys) A1AT misfolding

References

1. Gooptu, B. & Lomas, D.A. Conformational pathology of the serpins: themes, variations, and therapeutic strategies. *Annu Rev Biochem* **78**, 147–176 (2009).
2. Chapman, K.R., et al. Intravenous augmentation treatment and lung density in severe α 1 antitrypsin deficiency (RAPID): a randomised, double-blind, placebo-controlled trial. *Lancet* **386**, 360–368 (2015).
3. Teckman, J.H. & Jain, A. Advances in alpha-1-antitrypsin deficiency liver disease. *Curr Gastroenterol Rep* **16**, 367 (2014).
4. Yu, M.H., Lee, K.N. & Kim, J. The Z type variation of human α 1-antitrypsin causes a protein folding defect. *Nat Struct Biol* **2**, 363–367 (1995).
5. Novoradovskaya, N., Lee, J., Yu, Z.X., Ferrans, V.J. & Brantly, M. Inhibition of intracellular degradation increases secretion of a mutant form of α 1-antitrypsin associated with profound deficiency. *J Clin Invest* **101**, 2693–2701 (1998).
6. Teckman, J.H. & Perlmutter, D.H. Retention of mutant α 1-antitrypsin Z in endoplasmic reticulum is associated with an autophagic response. *Am J Physiol Gastrointest Liver Physiol* **279**, 961–74 (2000).
7. Kamimoto, T., et al. Intracellular inclusions containing mutant α 1-antitrypsin Z are propagated in the absence of autophagic activity. *J Biol Chem* **281**, 4467–4476 (2006).
8. Lomas, D.A., Evans, D.L., Finch, J.T. & Carrell, R.W. The mechanism of Z α 1-antitrypsin accumulation in the liver. *Nature* **357**, 605–607 (1992).
9. Kim, D. & Yu, M.H. Folding pathway of human α 1-antitrypsin: characterization of an intermediate that is active but prone to aggregation. *Biochem Biophys Res Commun* **226**, 378–384 (1996).
10. James, E.L., Whisstock, J.C., Gore, M.G. & Bottomley S.P. Probing the unfolding pathway of α 1-antitrypsin. *J Biol Chem* **274**, 9482–9488 (1999).
11. Dolmer, K. & Gettins, P.G.W. How the serpin α 1-proteinase inhibitor folds. *J Biol Chem* **287**, 12425–12432 (2012).
12. Tsutsui, Y., Dela Cruz, R. & Wintrode, P.L. Folding mechanism of the metastable serpin α 1-antitrypsin. *Proc Natl Acad Sci USA* **109**, 4467–4472 (2012).
13. Stocks, B.B., Sarkar, A., Wintrode, P.L. & Konermann, L. Early hydrophobic collapse of α 1-antitrypsin facilitates formation of a metastable state: insights from oxidative labeling and mass spectrometry. *J Mol Biol* **423**, 789–799 (2012).
14. Lindorff-Larsen, K., Piana, S., Dror, R.O. & Shaw, D.E. How fast-folding proteins fold.

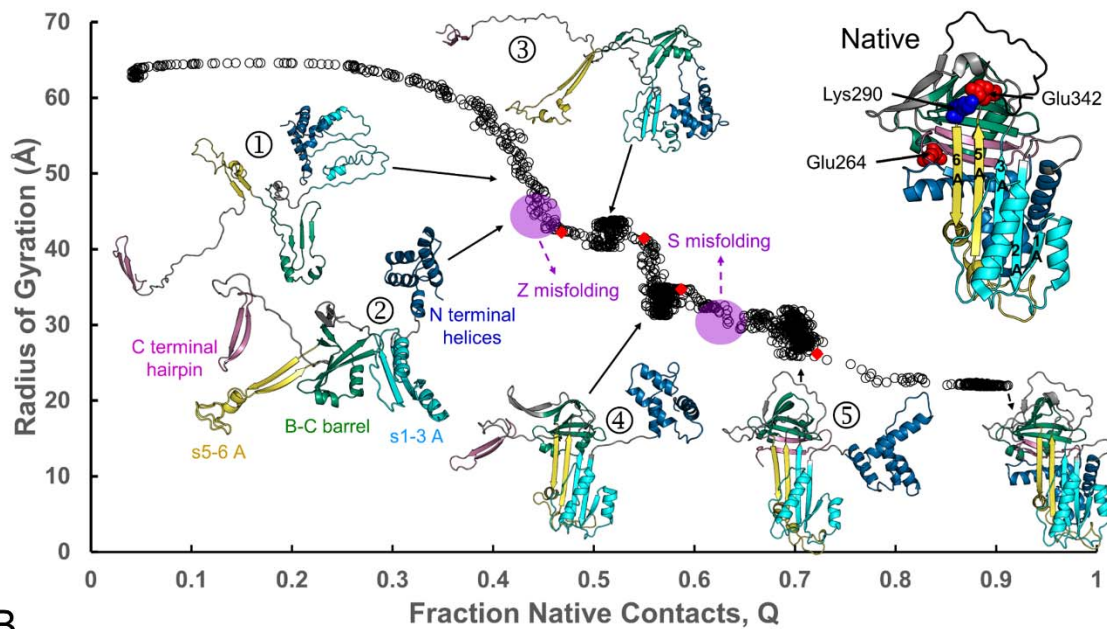
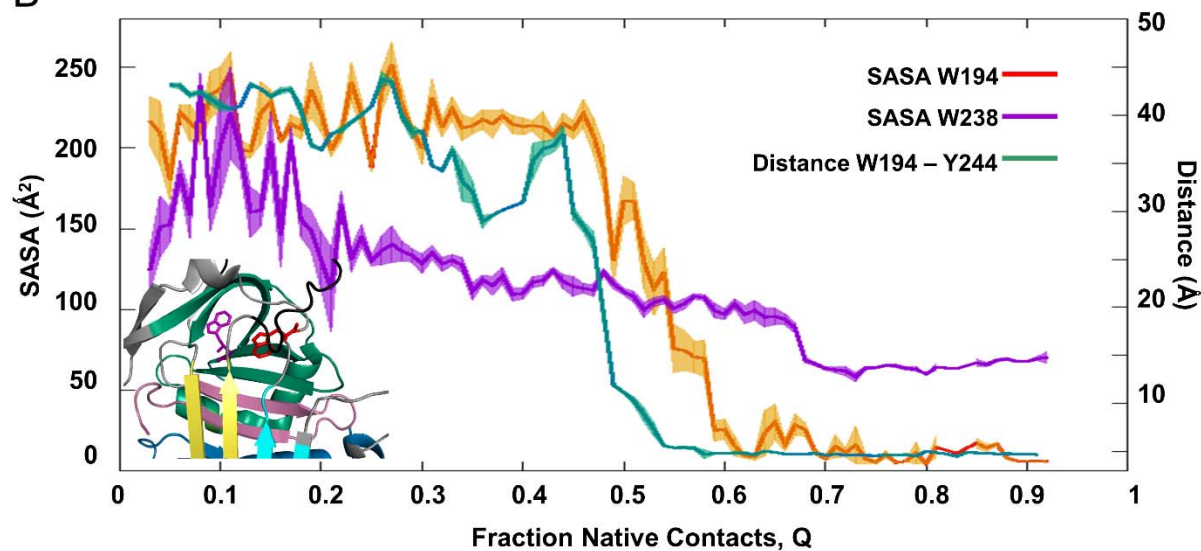
Science **334**, 517–520 (2011).

15. Bowman, G.R., Pande, V.S. & Noé, F. eds. *An introduction to Markov state models and their application to long timescale molecular simulation*. Advances in Experimental Medicine and Biology v. **797** (2013).
16. a Beccara, S., Fant, L. & Faccioli, P. Variational scheme to compute protein reaction pathways using atomistic force fields with explicit solvent. *Phys Rev Lett* **114**, 098103 (2015).
17. Paci, E. & Karplus, M. Forced unfolding of fibronectin type 3 modules: an analysis by biased molecular dynamics simulations. *J Mol Biol* **288**, 441–459 (1999).
18. Tiana, G. & Camilloni, C. Ratcheted molecular-dynamics simulations identify efficiently the transition state of protein folding. *J Chem Phys* **137**, 235101 (2012).
19. a Beccara, S., Skrbic, T., Covino, R. & Faccioli, P. Dominant folding pathways of a WW domain. *Proc Natl Acad Sci USA* **109**, 2330–2335 (2012).
20. Wang, F., Cazzolli, G., Wintrode, P. & Faccioli, P. Folding mechanism of proteins Im7 and Im9: insight from all-atom simulations in implicit and explicit solvent. *J Phys Chem B* **120**, 9297–9307 (2016).
21. Cazzolli, G., et al. Serpin latency transition at atomic resolution. *Proc Natl Acad Sci USA* **111**, 15414–15419 (2014).
22. Panchenko, A.R., Luthey-Schulten, Z. & Wolynes, P.G. Foldons, protein structural modules, and exons. *Proc Natl Acad Sci USA* **93**, 2008–2013 (1996).
23. Englander, S.W. & Mayne, L. The nature of protein folding pathways. *Proc Natl Acad Sci USA* **111**, 15873–15880 (2014).
24. Fan, Z., Dror, R.O., Mildorf, T.J., Piana, S. & Shaw D.E. Identifying localized changes in large systems: change-point detection for biomolecular simulations. *Proc Natl Acad Sci USA* **112**, 7454–7459 (2015).
25. Oktaviani, N. A., Risør, M. W., Lee, Y.-H., Megens, R. P., de Jong, D. H., Otten, R., et al. Optimized co-solute paramagnetic relaxation enhancement for the rapid NMR analysis of a highly fibrillogenic peptide. *J. Biomol. NMR*, **62**, 129–142 (2015).
26. Tew, D.J. & Bottomley, S..P Probing the equilibrium denaturation of the serpin α_1 -antitrypsin with single tryptophan mutants; evidence for structure in the urea unfolded state. *J Mol Biol* **313**, 1161–1169 (2001).
27. Onda, M., et al. Cleaved serpin refolds into the relaxed state via a stressed conformer. *J Biol Chem* **283**, 17568–17578 (2008).
28. Chandrasekhar, K., et al. Cellular folding pathway of a metastable serpin. *Proc Natl Acad*

Sci USA **113**, 6484–6489 (2016).

29. Brantly, M., Courtney, M. & Crystal, R.G. Repair of the secretion defect in the Z form of α_1 -antitrypsin by addition of a second mutation. *Science* **242**, 1700–1702 (1988).
30. Sifers, R.N., Hardick, C.P. & Woo, S.L. Disruption of the 290–342 salt bridge is not responsible for the secretory defect of the PiZ α_1 -antitrypsin variant. *J Biol Chem* **264**, 2997–3001 (1989).
31. Barducci, A., Bussi, G. & Parrinello, M. Well-tempered metadynamics: a smoothly converging and tunable free-energy method. *Phys Rev Lett* **100**, 020603 (2008).
32. Bolhuis, P.G., Chandler, D., Dellago, C. & Geissler, P.L. Transition path sampling: throwing ropes over rough mountain passes, in the dark. *Annu Rev Phys Chem* **53**, 291–318 (2002).
33. Escobedo, F.A., Borrero, E.E. & Araque, J.C. Transition path sampling and forward flux sampling. Applications to biological systems. *J Phys: Condens Matter* **21**, 333101 (2009).
34. West, A.M.A., Elber, R. & Shalloway, D. Extending molecular dynamics time scales with milestoning: example of complex kinetics in a solvated peptide. *J Chem Phys* **126**, 145104 (2007).
35. Lindorff-Larsen, K., et al. Improved side-chain torsion potentials for the Amber ff99SB protein force field. *Proteins* **78**, 1950–1958 (2010).
36. Hess, B., Kutzner, C., van der Spoel, D. & Lindahl, E. GROMACS 4: algorithms for highly efficient, load-balanced, and scalable molecular simulation. *J Chem Theory Comput* **4**, 435–447 (2008).
37. Elliott, P.R., Pei, X.Y., Dafforn, T.R. & Lomas D.A. Topography of a 2.0 Å structure of α_1 -antitrypsin reveals targets for rational drug design to prevent conformational disease. *Protein Sci* **9**, 1274–1281 (2000).
38. Humphrey, W., Dalke, A. & Schulter, K. VMD: visual molecular dynamics. *J Mol Graph* **14**, 33–38 (1996).
39. Huang, X., et al. Molecular mechanism of Z α_1 -antitrypsin deficiency. *J Biol Chem* **291**, 15674–15686 (2016).
40. Jorgensen, W.L., Chandrasekhar, J., Madura, J.D., Impey, R.W. & Klein, M.L. Comparison of simple potential functions for simulating liquid water. *J Chem Phys* **79**, 926–935 (1983).
41. Best, R.B., et al. Optimization of the additive CHARMM all-atom protein force field targeting improved sampling of the backbone φ , ψ and side-chain $\chi(1)$ and $\chi(2)$ dihedral angles. *J Chem Theory Comput* **8**, 3257–3273 (2012).

42. Essmann, U., et al. A smooth particle mesh Ewald method. *J Chem Phys* **103**, 8577–8593 (1995).

A**B****Figure 1.**

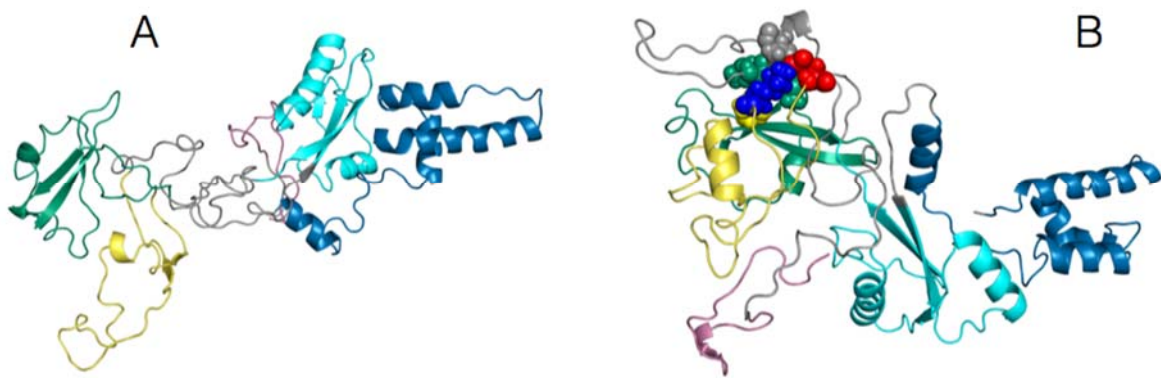


Figure 2.

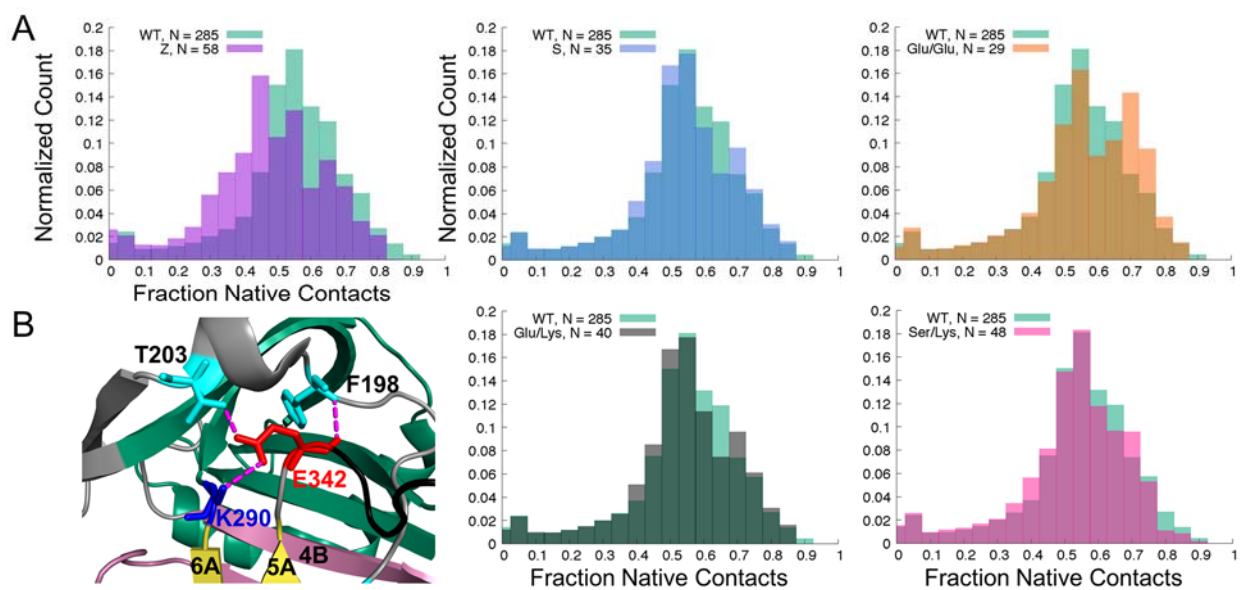


Figure 3.

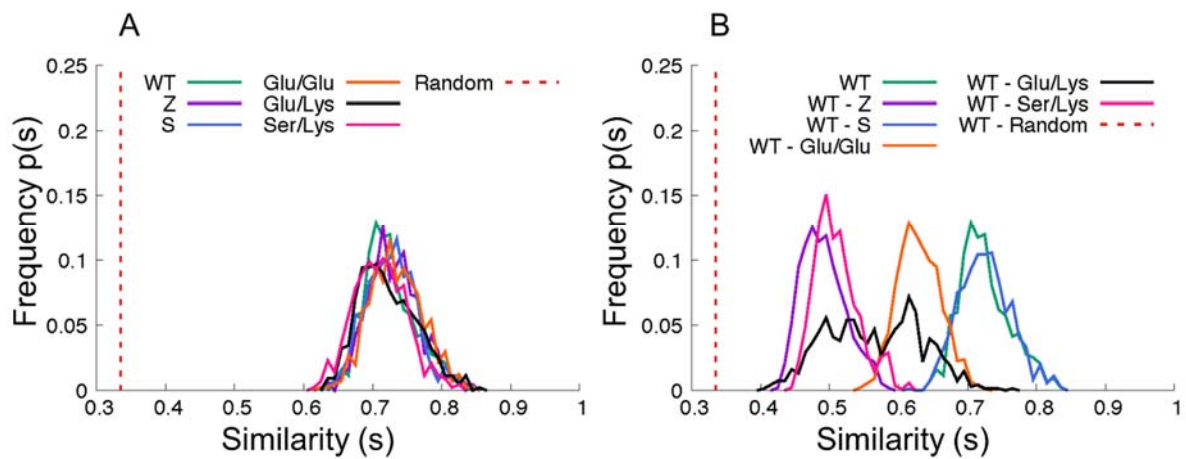


Figure 4.

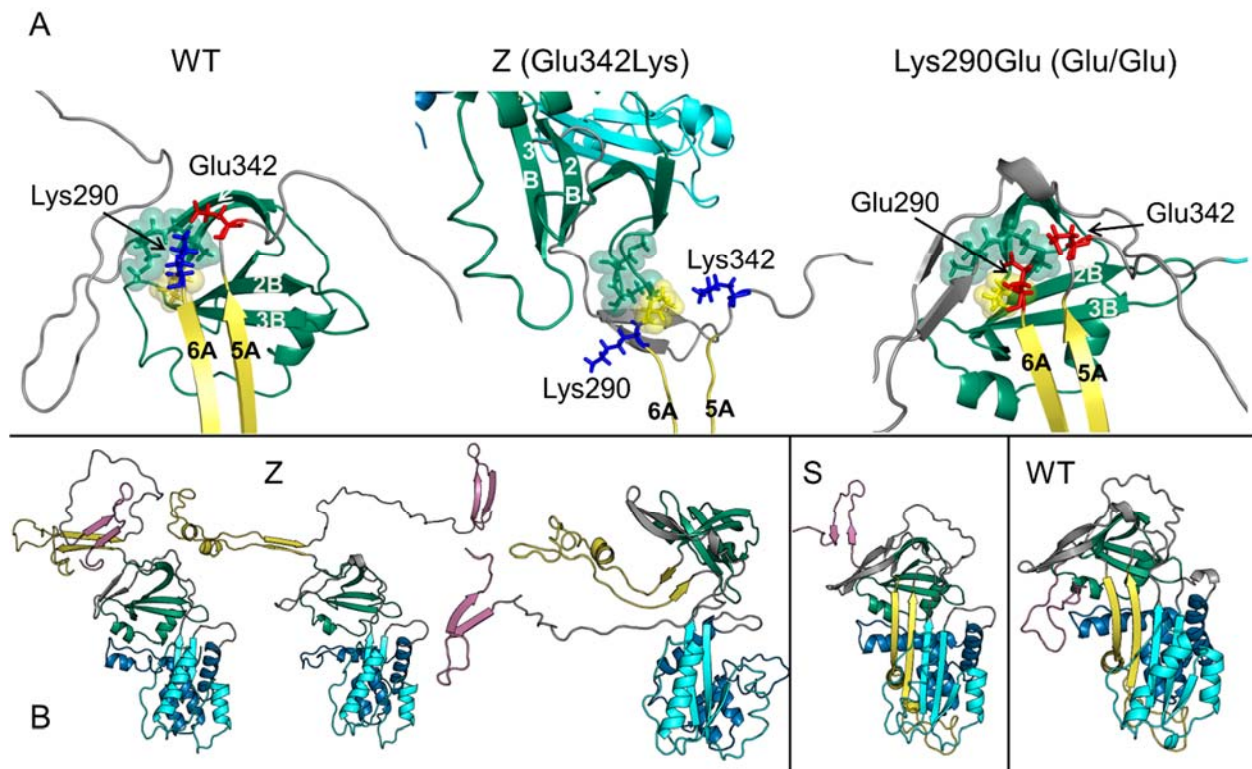


Figure 5.

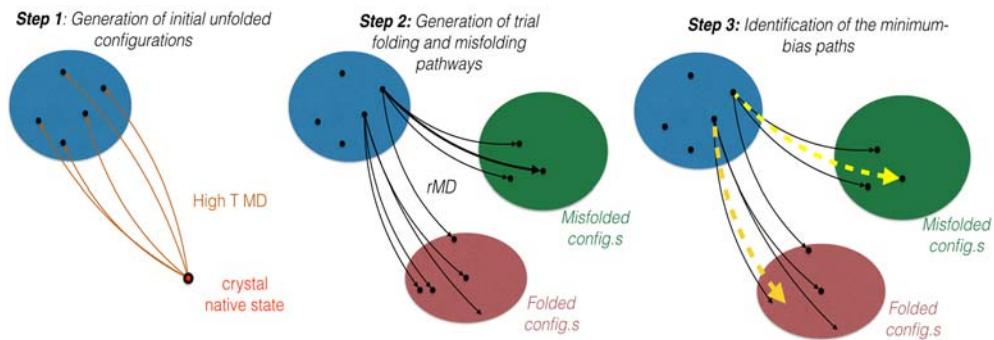


Figure 6.

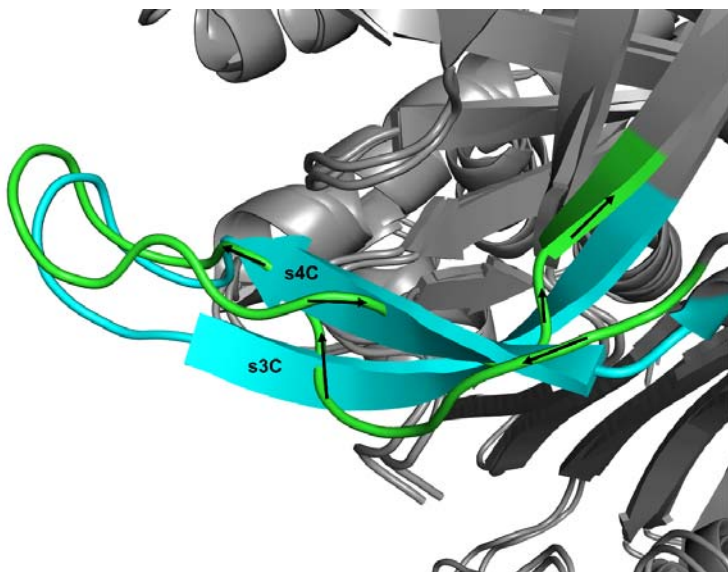


Figure 7.